Wet-Spinning of Continuous Montmorillonite-Graphene Fibers for Fire-Resistant Lightweight Conductors

Bo Fang,[†] Li Peng,[†] Zhen Xu,[†] and Chao Gao*[,†,‡]

[†]MOE Key Laboratory of Macromolecular Synthesis and Functionalization, Department of Polymer Science and Engineering, Zhejiang University, 38 Zheda Road, Hangzhou 310027, People's Republic of China and [‡]State Key Laboratory for Modification of Chemical Fibers and Polymer Materials, Donghua University, Shanghai 201620, People's Republic of China

ABSTRACT All-inorganic fibers composed of neat 2D crystals possessing fascinating performance (*e.g.*, alternately stacking layers, high mechanical strength, favorable electrical conductivity, and fire-resistance) are discussed in detail. We developed a wet-spinning assmebly strategy to achieve continuous all-inorganic fibers of montmorillonite (MMT) nanoplatelets by incorporation of a graphene oxide (GO) liquid crystal (LC) template at a rate of 9 cm/s, and the templating role of GO LC is confirmed by *in situ* confocal laser scanning microscopy and polarized optical microscopy inspections. After protofibers underwent thermal reduction, the obtained binary complex fibers composed of neat 2D crystals integrate the outstanding fire-retardance of MMT nanoplatelets and the excellent conductivity of graphene nanosheets. High-resolution transmission electron microscopy and scanning electron microscope observations reveal the microstructures of fibers with compactly stacking layers. MMT-graphene fibers show increaing tensile strengths (88−270 MPa) and electrical conductivities (130−10500 S/m) with increasing graphene fraction. MMT-graphene (10/90) fibers are used as fire-resistant (bearing temperature in air: 600−700 °C), lightweight ($\rho < 1.62$ g/cm^3) conductors (conductivity: up to 1.04×10^4 S/m) in view of their superior performance in high-temperature air beyond commercial T700 carbon fibers. We attribute the fire-resistance of MMT-graphene fibers to the armor-like protection of MMT layers, which could shield graphene layers from the action of oxidative etching. The composite fibers worked well as fire-resistant conductors when being heated to glowing red by an alcohol lamp. Our GO LC-templating wet-spinning strategy may also inspire the continuous assembly of other layered crystals into high-performance composite fibers.

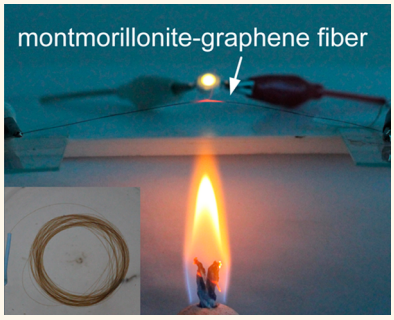

KEYWORDS: wet-spinning · 2D crystals · liquid crystal · self-templating · fire-resistance · lightweight · conductor

Atomically thin 2D crystals including clay, graphene, and graphene-like 2D crystals have shown fascinating mechanical, electrical, and thermal attributes.[1−4] But harnessing such properties requires finding a way to turn these nanoscale tiny flakes into macroscopic-scale materials. Given the high melting points of inorganic compounds, fluid assembly is the sole industrially viable approach to cost-effective fabrication of macroscopic ordered materials. Hitherto, parts of 2D crystals have been successfully assembled into multidimensional macrostrucrures by solution-based methods. For instance, layer-by-layer deposition,[5,6] vacuum-assisted filtration[7,8] and Langmuir−Blodgett[9,10] strategies have given birth to small-size films/papers with the assistance of adhesive matter (*e.g.*, polymer), and 3D macroarchitectures have also been fabricated by hydrothermal treatment[11,12] or direct lyophilization[13,14] from 2D crystal suspensions. The obtained macroscopic materials usually own hierarchical microstructures and fantastic properties translated from the inherent attributes of 2D building blocks.[15] However, it is almost impossible for such methods to access continuous materials, especially fibers, limiting their real applications in practice.

Wet-spinning assembly has been demonstrated as a versatile strategy to fabricate continuous graphene fibers.[16−20] However, no reports on wet-spun fibers of other 2D crystals have been published. A key point of assembling continuous fibers from 2D crystals is to ensure their self-supporting

* Address correspondence to chaogao@zju.edu.cn.

Received for review January 28, 2015 and accepted April 20, 2015.

Published online April 20, 2015
10.1021/acsnano.5b00616

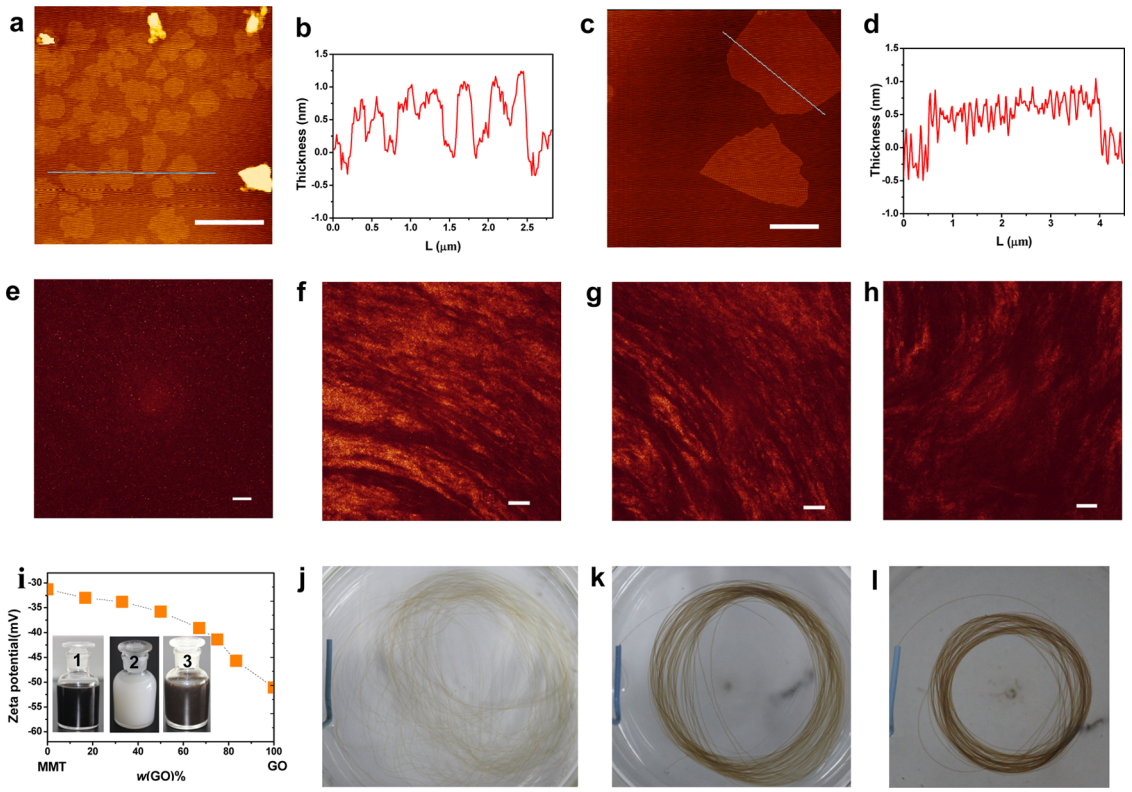

Figure 1. AFM images and heights of MMT nanoplatelets (a, b) and GO nanosheets (c, d) deposited on mica. Confocal laser microscopy observations of an slMMT suspension (e) and MMT-GO 80/20 (f), 40/60 (g), and 10/90 (h) hybrid suspensions. (i) Zeta potential of MMT-GO composite dispersions as a function of GO concentration. Inset: (1) GO solution, (2) slMMT dispersion, and (3) MMT-GO suspension after standing for one month. The wet-spun MMT-GO protofibers, with weight ratios of MMT/GO of 80/20 (j), 40/60 (k), and 10/90 (l), respectively. Scale bars: (a) 1 μm, (c) 2 μm, (e) 20 μm, (f–h) 40 μm.

organization once being wet-spun from a fluid-phase system, which still remains a challenge for general nanosheets due to their low solubility, their weak interlaminar attractions, and the absence of molecular entanglement in their suspensions.

Herein, we achieve for the first time all-inorganic wet-spun fibers of montmorillonite (MMT) nanoplatelets by incorporation of a graphene oxide (GO) liquid crystal (LC) template. The loading (down to 20 wt %) of GO LCs guarantees the spinnability of MMT-GO hybrid suspensions. High-temperature treatment reduces MMT-GO protofibers to MMT-G (MMT-graphene) fibers. These binary complex fibers composed of pure 2D crystals integrate the outstanding thermostability of MMT and the excellent conductivity of graphene. The introduction of 10 wt % MMT enables MMT-G fibers to show a high decomposition temperature ($T_{d,95}$, 612 °C) in air and high residual mass fracture (f_{rm}, 97.09%) at 600 °C, which is obviously superior to the corresponding $T_{d,95}$ (561 °C) and f_{rm} (89.31%) of commercial T700 carbon fibers. The lightweight MMT-G (10/90) fibers with a density of 1.62 g/cm^3 exhibit high electrical conductivity (3500 S/m) and good mechanical and volumetric stabilities after 1 h of thermal treatment at 600 °C in air. The MMT-G (10/90) fibers work well as fire-resistant, lightweight conductors when heated to glowing red by an alcohol lamp.

RESULTS AND DISCUSSION

Wet-Spinning Doping of MMT-GO LC. Experimentally, the high exfoliation degree of 2D crystals is necessary for their continuous assembly because aggregated particles likely form defects in fiber bulk and compromise physical properties. The clay crystals of Na^+ MMT are checked by X-ray powder diffraction, shown in Figure S1. We exfoliated the bulky MMT into single-layer MMT (slMMT) aqueous suspensions by vigorous stirring and ultrasonication. The AFM measurements demonstrated the single-layer state and individual dispersion of slMMT nanoplateletes with a thickness of 1.0 nm and average lateral size of 293 nm (Figure 1a,b). Ultralarge single-layer GO nanosheets with a thickness of 0.8 nm and average lateral size of 15 μm were commercially available from C6G6 (Figure 1c,d). The high aspect ratios (~1.9 × 10^4) of GO could facilitate the formation of LCs at very low concentration (for example, 1 mg/mL), making it possible to play the templating role of GO LCs in a broad concentration range.[21]

In situ confocal laser scanning microscopy (CLSM) observations and polarized optical microscopy (POM) inspections revealed the templating role of GO LCs in MMT-GO hybrid suspensions. GO sheets are fluorescent under visible light,[22] but MMT nanoplatelets are not due to the absence of fluorescent groups.

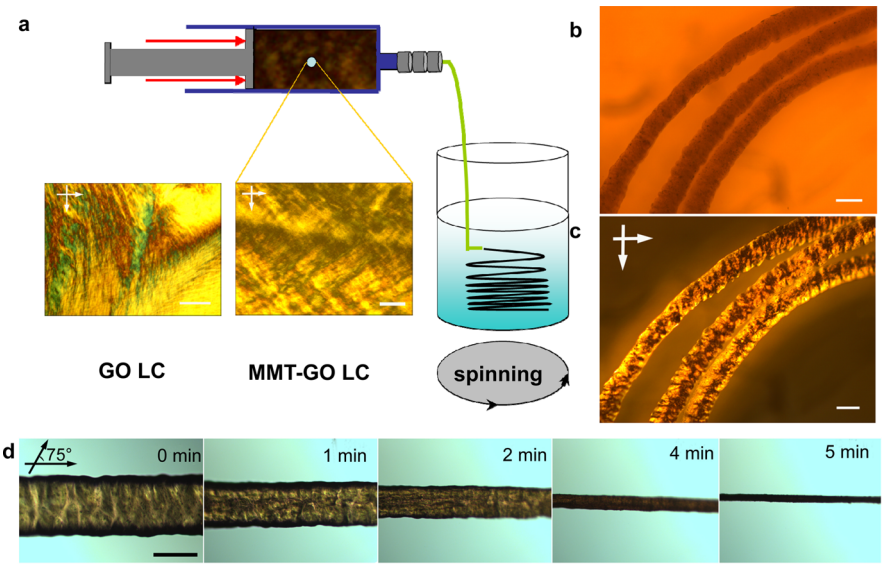

Figure 2. (a) Schematic illustration of wet-spinning of MMT-GO gel fibers and *in situ* POM images showing the LC behavior of GO and MMT-GO suspensions. Optical microscopic image (b) and POM image (c) of MMT-GO gel fibers in a coagulation bath. (d) Formation of MMT-GO fibers in air under the observation of 75° cross-polarized microscopy. Scale bars in a, b, c, and d are 200 μm.

To guarantee the direct CLSM inspection of the distribution of slMMT nanoplatelets in aqueous solution, we stained MMT with Auramine O (the detailed protocol is described in the Experimental Methods).[23] As shown in Figure 1e, the dispersion of slMMT nanoplateles with a concentration of 5 mg/mL is isotropic at the real-time state (pH ~7), in accordance with general rigid colloid suspensions.[24,25] In the case of MMT-GO hybrid suspensions, GO nanosheets form nematic LCs in different weight ratios. As discerned in Figure 1f–h, the formation of ring-like textures is caused by the polarized nature of the laser source and the variational orientational vectors of GO LCs in adjacent domains,[19] while slMMT nanoplatelets that display sparkling spots disperse uniformly in the interlayer channels of nematic domains. In turn, the confining effect of GO LCs on slMMT eliminates the chance of phase separation in spinning dopes, providing uniform distribution of mixing 2D building blocks in binary fibers. POM examinations also confirmed the LC behavior of MMT-GO in a large magnification (see Figure S2). Notably, along with the introduction of GO, larger nematic domains with fewer defects were observed in the hybrid suspensions, offering an opportunity to fabricate fibers with higher microstructural regularity and better physical performance.

Reliable dispersive stability is of great importance for the scalable fluid assembly of 2D nanoparticles. Quantitatively, the dispersive stability of the MMT-GO hybrid suspension was studied by zeta-potential measurements, as shown in Figure 1i. Traversing the zeta-potential diagram from left to right (low loading to high loading of GO), the zeta-potential value decreased gradually upon the addition of GO, down to −52 mV, which was the value of neat GO dispersions. Furthermore, after allowing GO (inset 1 in Figure 1i), slMMT (inset 2 in Figure 1i), and MMT-GO hybrid (inset 3 in Figure 1i) aqueous suspensions to stand for one month, no sediments appeared in the bottoms of the containers. Such a superb dispersive stability of MMT-GO hybrid aqueous suspensions facilitates the formation of continuous fibers. Consequently, direct wet-spinning of the MMT-GO spinning dope resulted in dozens of meters long continuous fibers with the proportion of slMMT from 80 to 10 wt % in a matter of seconds (about 9 cm/s) on a homemade wet-spinning apparatus (Figure 1j–l).

Wet-Spinning of Continuous MMT-GO Fibers. Figure 2a depicts the wet-spinning assembly procedure to fabricate MMT-GO protofibers from MMT-GO LCs. Simply stated, MMT-GO hybrid suspensions (at a concentration of 5 mg/mL) were extruded through a narrow spinning nozzle with an inner diameter of 250 μm and then soaked in a $CaCl_2$ coagulation bath (Ca^+ ion induces an electrostatically interlinked network among slMMT nanoplatelets and GO nanosheets).[21] Shear flow, colloidal interactions, and solvent removal facilitated the formation of protofibers, displaying a gel state under the *in situ* inspection of optical microscopy (Figure 2b). Birefringence shown in Figure 2c identified the oriented alignment of building blocks in the protofiber interior. The gel fiber edges appeared brighter than its centers since strong shear flow (occurring in the vicinity of the spinning nozzle inner wall) drove the prealignment of nanoparticles along the axis of the protofiber. Water-washing and air-drying allowed swollen protofibers to evolve into neat MMT-GO fibers, and the corresponding time dependence of microstructure

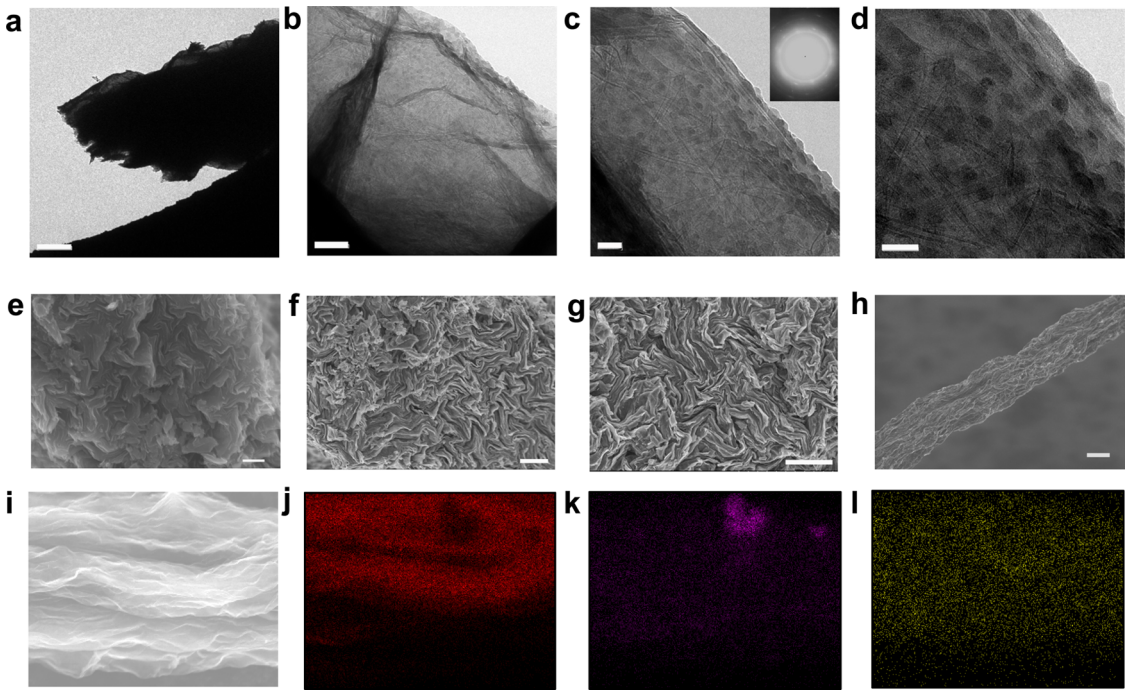

Figure 3. HRTEM images of a representative MMT-G fiber (a−d). The inset in (c) shows the SAED pattern of the MMT-G fiber. SEM images of the cross section of an MMT-G (80/20) fiber (e), MMT-G (40/60) fiber (f), and MMT-G (10/90) fiber (g). SEM images of the surface section of a G-MMT fiber (h, i) and its corresponding C-element mapping (j), Si-element mapping (k), and Al-element mapping (l). Scale bars: (a) 5 μm; (b) 0.2 μm; (c) 100 nm; (d) 50 nm; (e, g) 2 μm; (f) 1 μm; (h) 4 μm.

evolution was ascertained under 75° cross-polarized microscopy (see Figure 2d). Initially, water remained in the gel fibers, and thus vivid nematic textures could still be discerned (as indicated by the POM observations in Figure S3). The rapid solvent removal induced peristaltic modulations at the surfaces, which unbent gradually following the drying and stretching process. After ~5 min, about 13 μm high compact thick MMT-GO fibers (about 1/20 of the protofiber) formed. XRD patterns (see Figure S4) showed the interlayer spacing of MMT-GO fibers (8.8 Å for 40 wt %, 8.56 Å for 10 wt %) decreased along with introduction of GO, larger than that of neat GO fibers (8.11 Å). The as-prepared insulating MMT-GO fibers were transformed into electrically conductive MMT-G fibers by 2 h thermal treatment at 800 °C under nitrogen, due to the removal of oxygen-containing groups and restoration of conjugated nets in graphene nanosheets. As confirmed by the XPS spectra in Figure S5, the vanishing of epoxy/hydroxyls (O−C═O, 289.2 eV; C═O, 288 eV; C−O, 287 eV) accompanied the drastic increasing of C−C/C═C bonds (C sp^2, 284.7 eV; C sp^3, 285.5 eV).

High-resolution transmission electron microscopy (HRTEM) and scanning electron microscope (SEM) distinctly revealed the surface and interior of MMT-G fibers. Since MMT nanoplatelets are composed of heavier elements (Al, Si, and O) than surrounding graphene (C), they appear darker in bright-field HRTEM images.[26] MMT nanoplatelets and graphene nanosheets stacked alternately and uniformly under the observations of HRTEM perpendicular to the surface of the MMT-G fiber (Figure 3a−d), and the uniformity of MMT was almost perfect. High-temperature treatment reduced the lateral size of MMT nanoplatelets (~50 nm), blamed for the loss of structural water through dehydroxylation in the margins.[27] Nevertheless, the crystalline nature (as indicated by the concentric diffraction ring shown in the SAED pattern) and the excellent physical properties of MMT-G fibers (as discussed hereinafter) indicated that the decreasing size did not decrease the intrinsic merits of MMT nanoplatelets. The cross section of an MMT-G fiber (Figure 3e−g), composed of binary 2D building blocks in nanoscale, exhibited compactly stacked multilayers, taking shape in the oriented alignment of the building blocks in MMT-GO LCs and enhanced by the postprocessing and thermal treatment of MMT-GO fibers. The surface presented uniformly arranged wrinkles parallel to the fiber axis (Figure 3h-,i), and energy-dispersive spectroscopy (EDS) mapping images of the fiber surface (Figure 3j−l) (see EDS mapping images of the cross section in Figure S6) illustrated the uniform distribution of MMT nanoplatelets and graphene nanosheets in MMT-G fibers.

Mechanical and Electrical Properties of MMT-G Fibers. Generally, the mechanical and electrical performances of macroscopic nanocomposites fibers were translated from single nano-object properties. In the MMT-G fibers, flexible graphene nanosheets dominate the electrical conductivity and tensile strength ($\pi-\pi$ interactions between graphene nanosheets surpass the van der Waals interactions of MMT nanoplatelets and the

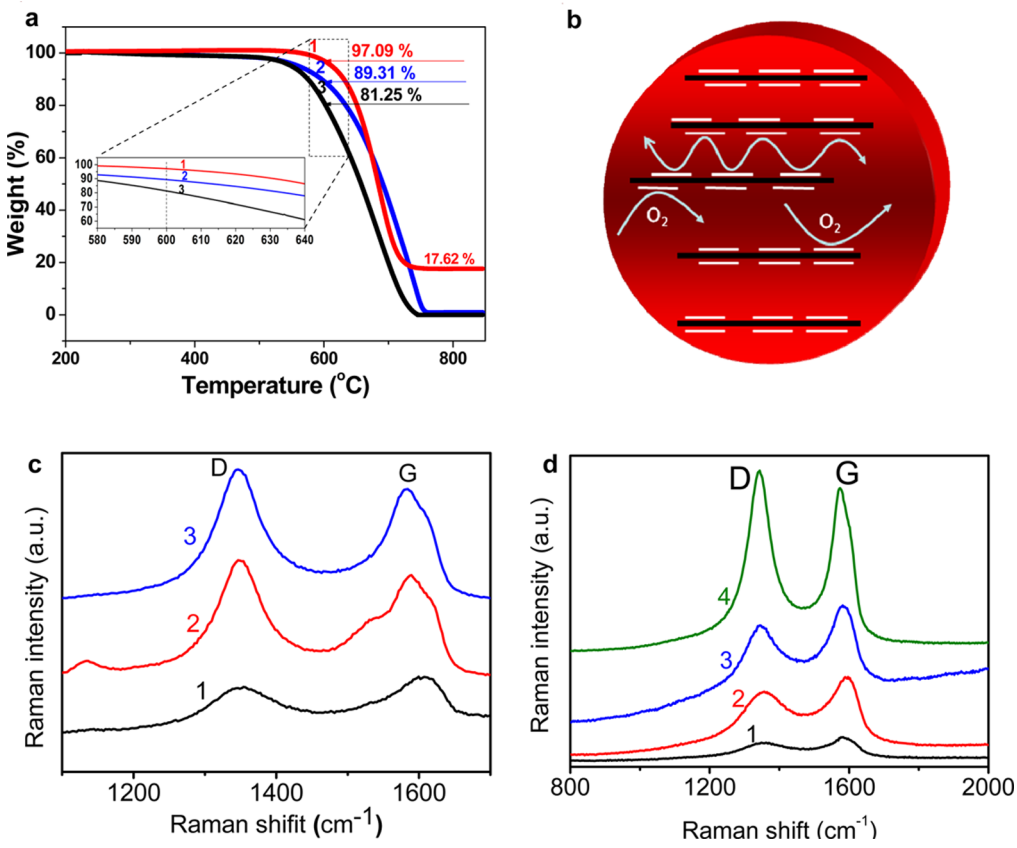

Figure 4. (a) TGA curves of MMT-G (10/90) fibers (1), T700 (2), and neat graphene fibers (3) in air. (b) Scheme showing that inorganic MMT nanoplatelets (white rectangles) shield graphene nanosheets (black rectangles) from the attack of oxygen when fibers (crimson cylinders) are heated in high-temperature air. (c) Raman spectra of neat graphene fibers at room temperature (1) and after 400 °C (2) and 500 °C (3) heating for 1 h in air. The corresponding I_D/I_G intensity ratio is 0.8 (1), 1.12 (2), and 1.16 (3). (d) Raman spectra of the MMT-G (10/90) fibers at room temperature (1) and after 400 °C (2), 500 °C (3), and 600 °C (4) heating for 1 h in air. The corresponding I_D/I_G intensity ratio is 0.79 (1), 0.81 (2), 0.84 (3), and 1.09 (4).

hydrogen-bonding interactions between all the building blocks).[21] With increasing graphene fraction, the tensile strength (88−270 MPa) and electrical conductivity of MMT-G fibers (130−10500 S/m) gradually increased, while keeping high Young's moduli (44−25 GPa), as shown in Figure S7 and Table S1. In the case of tensile strength, MMT-G hybrid fibers were much stronger than the nacre-like bionanocomposite films fabricated from clay and PDDA[5] or chitosan.[8] *In situ* SEM observation of the jagged fracture tips (Figure S8) under tensile measurement showed the pulled-out graphene sheets, implying that the deformation mechanism of MMT-G fibers is a tension-shear model, a prevalent theory for nanocomposites.[28,29] The MMT-G (80/20) fibers possessed a conductivity of 130 S/m, ~4.5-fold that of a highly oriented MMT-G hybrid film (28.6 S/m) in the same weight ratio.[30] Indeed, the MMT-G fibers at high MMT content still retain good flexibility. For example, the SEM images in Figure S9 show that a single MMT-G (80/20) fiber is easily bent into circles and twisted into strands. It is worth noting that the tensile strength (270 MPa) and conductivity (1.04×10^4 S/m) of MMT-G (10/90) fibers are highly approaching those of neat graphene fibers (286 MPa, 1.05×10^4 S/m, respectively), suggesting there is an apparent advantage to using MMT-G (10/90) fibers as practical conductors.

Thermostability of MMT-G (10/90) Fibers. MMT has been widely used to improve the thermostability of polymer-based nanocomposites in air, due to its excellent barrier properties.[31−33] On the contrary, graphene sheets or graphite are susceptible to oxidative etching in high-temperature air.[34] Thermogravimetric analyses illustrated the thermal degradation curves of T700, neat graphene fibers, and MMT-G (10/90) fibers in air, with a heating rate of 10 °C min^{-1} (Figure 4a). The MMT-G (10/90) fiber shows a $T_{d,95}$ of 612 °C, higher than that of T700 (561 °C) by around 51 °C and neat graphene fibers (550 °C) by about 62 °C. At 600 °C, the instant amount of residue is 97.09% for MMT-G (10/90) fibers, whereas only 89.31% for T700 and 81.25% for neat graphene fibers, suggesting a slower oxidative degradation of MMT-G (10/90) fibers. The residual weight percentage of MMT-G (10/90) fibers at 800 °C is 17.62%, more than the original weight percentage of MMT (10%), partly because the graphene fraction decreases with the removal of oxygen-containing groups on GO after reduction treatment.

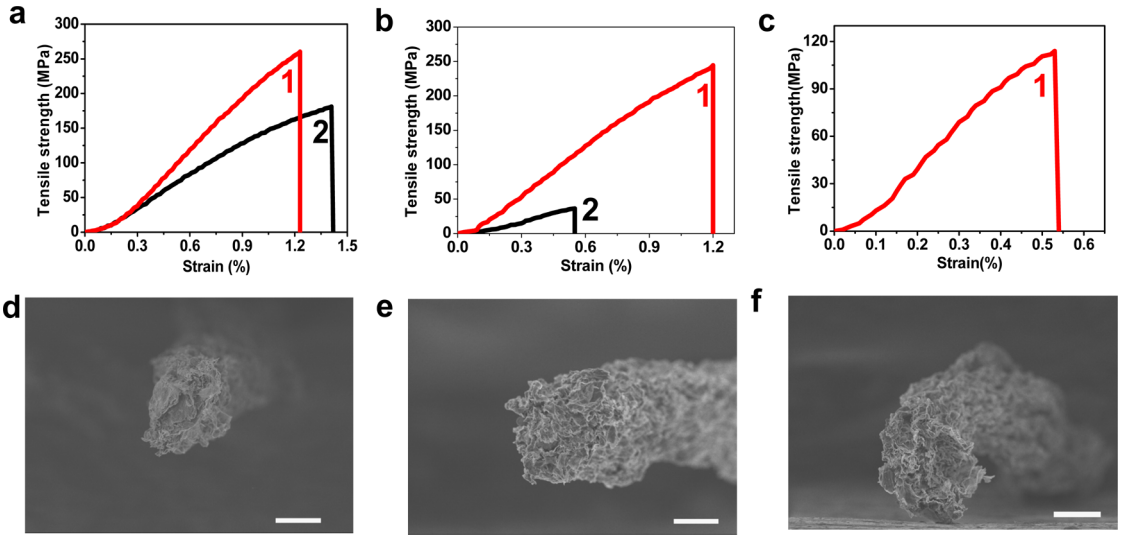

Figure 5. Typical mechanical measurements under tension for MMT-G (10/90) fibers (1) and neat graphene fibers (2) after 400 °C heating (a), 500 °C heating (b), and 600 °C heating (c) in air for 1 h and the corresponding cross sections (d, e, f, respectively). Scale bars: (d) 10 μm; (e) 5 μm; (f) 10 μm.

Thermostability Mechanism of MMT-G (10/90) Fibers. We mainly attribute the fine thermostability of MMT-G fibers to the gas-barrier properties of MMT nanoplatelets (Figure 4b). In high-temperature (such as 400 °C) air, ground-state triplet O_2 evolves into excited singlet O_2, which tends to form covalent bonds with carbon atoms, resulting in nanoscale etch pits and lattice disorders in graphene.[34] Raman spectroscopy is an effective method to study the lattice disorders of graphene. Here, the Raman spectra of neat graphene fibers and the MMT-G (90/10) fibers after different temperature (400−500 °C) treatment are shown in Figure 4c,d. The band at around 1340 cm^{-1} is ascribed to the D band, showing the vibrations of sp^3 carbon atoms of disorders; the band at about 1585 cm^{-1} is related to the G band, reflecting the vibrations of sp^2 carbon atoms in the hexagonal lattice of graphene. The ratio of the intensity of the D and G band (I_D/I_G) is in direct proportion to disordered degree of the graphene lattice. At room temperature, the value of I_D/I_G for neat graphene fibers (0.80) is very close to that of MMT-G (10/90) fibers (0.79). After thermal treatments, the I_D/I_G of neat graphene fibers increases greatly to 1.12 at 400 °C and to 1.16 at 500 °C, indicating the expansion of lattice disorders in graphene caused by oxidative etching. In comparison, the corresponding value of I_D/I_G for the MMT-G fibers rises only slightly to 0.81 at 400 °C and to 0.84 at 500 °C, much smaller than those of neat graphene fibers. These results demonstrate that the incorporation of MMT nanoplatelets effectively stabilizes graphene lattice structure in high-temperature air, mainly because MMT nanoplatelets obstruct the contact of singlet O_2 with carbon atoms.

As revealed by previous reports, gas molecules are unable to permeate MMT nanoplatelets.[26] MMT/polymer nanocomposites exhibit excellent barrier properties, since MMT layers compel the permeating gas molecules to wiggle around them in tortuous paths.[35−39] Zeng *et al.* reported the permeation of O_2 decreased to half that of a pure PET film when 3 wt % MMT was introduced.[40]

HRTEM observations in Figure 3b−d confirm that MMT-G fibers are composed of alternately stacking layers, namely, MMT layers and graphene layers. As shown in Figure 4b, when heating occurs in air, the inorganic MMT layers, acting as armor layers, shield graphene from the action of singlet O_2 and reduce the chance of the formation of etch pits. Decreasing etch pits means a longer lifetime of graphene layers inside a fire. This armor-like protection naturally assists graphene fibers to show favorable performance after undergoing long-time and high-temperature baking in air, such as high electrical conductivities and fine mechanical and volumetric stabilities. This explanation is supported by the tracking records of physical parameters of the MMT-G (10/90) fibers and neat graphene fibers at stepwise rising temperatures, as discussed hereinafter.

Mechanical and Volumetric Stabilities of MMT-G (10/90) Fibers. The mechanical measurements under tension for MMT-G (10/90) fibers and neat graphene fibers were conducted at every 100 °C increment up to 700 °C in air. After baking for 1 h at 400 °C in air, the typical tensile strength of MMT-G (10/90) fibers decreased slightly to 260 MPa, while that of neat graphene fibers declined sharply to 181 MPa (see Figure 5a). After further heating at 500 °C for 1 h, the MMT-G (10/90) fibers weaken to 245 MPa, 680% of neat graphene fibers (36 MPa) (Figure 5b). Figure 5d,e show that the cross-section microstructures of MMT-G (10/90) fibers maintained a high integrity and regularity after

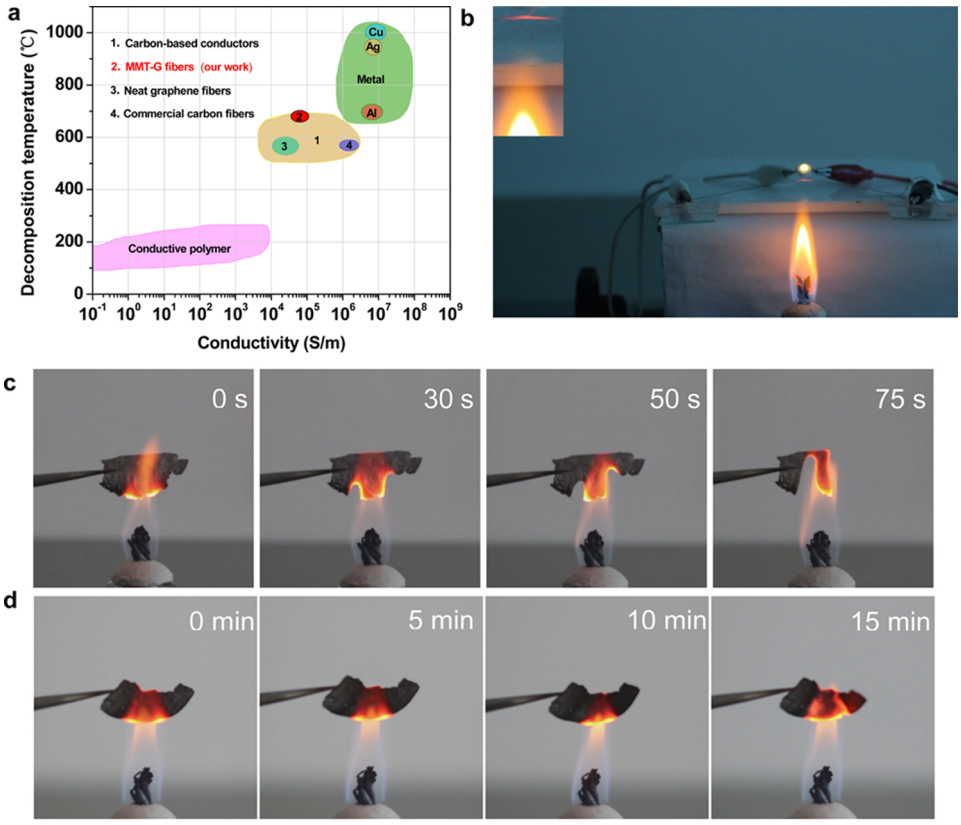

Figure 6. (a) Ashby plot comparing the MMT-G (10/90) fibers with other relevant fire-retardant conductors. (b) Circuit constructed by an LED chip and twisted MMT-G (10/90) fibers. The LED chip works well when the fibers are heated to glowing red, and the inset highlights the glowing red part. The combustion progress of neat graphene films (c) and MMT-G films (d) in air.

400 and 500 °C heating, in accordance with their corresponding Raman spectral analysis in Figure 4c. When the temperature was increased to 600 °C for another 1 h, neat graphene fibers lost volumetric stability without residue, while the MMT-G (10/90) fibers still retained high mechanical strength (113 MPa) (Figure 5c) and maintained their self-standing shape and flexibility (Figure 5f). The MMT-G (10/90) fibers fragmented into black powders after 1 h at 700 °C, suggesting the bearing temperature of MMT-G (10/90) fibers is 600−700 °C. More variations of related physical properties are listed in Table S2. The value of I_D/I_G of MMT-G (10/90) fibers increased to 1.09 after 600 °C baking (see Figure 4c), implying lattice distortions induced by oxidation on graphene sheets, but the conjugated nets were partly preserved, which was proved by their high conductivity (3500 S/m). The preservation of conjugated nets in graphene sheets and favorable electrical conductivities of MMT-G (10/90) fibers affirmed the armor-like shielding function of MMT layers on the graphene layers. In addition, the density of MMT-G (10/90) fibers changed from 1.38 g/cm^3 (at room temperature) to 1.62 g/cm^3 (after 1 h baking in 600 °C air), less than that of T700 (~2.2 g/cm^3) and other alloy conductors. These results highlighted the superb enhancing thermal stability of MMT, which could not only remarkably improve the mechanical and volumetric stabilities of graphene fibers but also permit the MMT-G (10/90) fibers to work as lightweight conductors in high-temperature air.

Lightweight and Fire-Resistant Conductors of MMT-G (10/90) Fibers. We provide an Ashby plot (Figure 6a) to compare the MMT-G (10/90) fibers with other fire-resistant conductors. The MMT-G (10/90) fibers are expected to behave better than conductive polymer materials for use as conductors in high-temperature air. Even though the MMT-G fibers perform less well than metallic conductors, their ultralow density (ρ < 1.62 g/cm^3) make them superior to metal (6−10 g/cm^3) in the field of lightweight materials. We also checked the real performance of MMT-G (10/90) fibers in a combustion environment. As shown in Figure 6b, we twisted dozens of fibers compactly together and bound them on conductive clips to construct a working-well circuit (see full view in Figure S10). Then an alcohol lamp (an alcohol lamp was chosen because its outer flame temperature is close to the bearing temperature of MMT-G (10/90) fibers) was used to heat and burn the MMT-G (10/90) fibers directly. Although the combusted part became glowing red (inset in Figure 6b), the MMT-G (10/90) fibers still worked well to light the LED chip. The combustion contrast of the MMT-G film and neat graphene films further verified the outstanding fire-resistant performance of the MMT-G

nanocomposites. As Figure 6c,d show, the MMT-G film holds its shape under combustion for 15 min (recorded in movie S1), whereas neat graphene films are burned in seconds (recorded in movie S2).

CONCLUSIONS

We realized the first wet-spinning assembly of MMT 2D crystals with the introduction of a GO LC solution. The LC behavior of MMT-GO hybrid suspensions, the assembly mechanism of MMT-G fibers, and their physical properties were explained in detail. The MMT-G (10/90) fibers possess favorable electrical conductivity and better volumetric stability and mechanical stability than neat graphene fibers in high-temperature air. Such integrated merits guarantee the use of MMT-G (10/90) fibers as lightweight fire-resistant conductors. Considering the similar fluid-phase behavior of MMT to other 2D layered materials (MoS_2, WS_2, $MoSe_2$, $TaSe_2$, $NbSe_2$, $NiTe_2$, BN, Bi_2Te_3 *etc.*) and the superb solubility of GO in common polar solvents, our LC-templating wet-spinning strategy is in principle applicable to any kind of 2D crystal. This provides a general avenue for continuous fluid assembly of layered crystals to access high-performance multifunctional composite fibers.

EXPERIMENTAL METHODS

Materials. Ultralarge single-layer GO nanosheets with a thickness of 0.8 nm and average lateral size of 15 μm were commercially available from C6G6 (www.c6g6.com) and used as received. Sodium montmorillonite powder was donated by Zhejiang Fenghong New Materials Co., Ltd.

Preparation of MMT-GO Hybrids. The GO aqueous dispersion was purchased from C6G6 (www.c6g6.com).[41] The aqueous suspension of MMT was obtained by dissolving 3 g of Na-MMT in 300 mL of deionized water. After vigorously stirring for 15 days followed by 6 h of ultrasonication, the obtained solution was left standing for 1 day to allow deposition of undissolved clay. Desired amounts of obtained MMT suspension were added into the GO solution, to make sure that the concentration of the mixture was 5 mg/mL. After stirring for 30 min, the mixture was sonicated for 1 h. A homogeneous dispersion of MMT-GO was finally obtained.

Fluorescence Staining of slMMT with Auramine O. Auramine O powder was dispersed into slMMT suspensions with a dye concentration of 2.5×10^{-6} M. The hybrid dispersions were stirred for 10 min to guarantee the sufficient absorption of Auramine O molecules on the MMT nanoplatelets. After undergoing low-speed centrifugation (2500 rpm), unabsorbed Auramine O molecules was washed away, and the obtained homogeneous suspensions were used for CLSM observations.

Wet-Spinning of MMT-G Fibers. The ready MMT-GO hybrid dispersion was loaded into a 5 mL plastic syringe with a spinning nozzle (PEEK tube with a diameter of 250 μm) and injected into a $CaCl_2$ bath (8 mg/mL) by an injection pump (100 mL min^{-1}). The newly formed fibers were drawn out and collected on a scroll and dried for 12 h at 40 °C under air. The dried fibers were heated in a tube furnace for 2 h at 800 °C under nitrogen. After the tube furnace cooled, MMT-G fibers were obtained.

Characterization. POM observations were performed with a Nikon E600POL. SEM images were taken on a Hitachi S4800 field-emission SEM system. AFM images of GGO sheets and MMT nanoplatelets were taken in the tapping mode on an NSK SPI3800, with samples prepared by spin-coating from diluted aqueous solutions onto freshly exfoliated mica substrates at 1000 rpm. HRTEM images of fibers were taken on a JEM-2010 HR-TEM. Thermogravimetric analysis (TGA) was carried out on a PerkinElmer Pyris 6 TGA instrument under air with a heating rate of 10 °C min^{-1}. All electrical transport properties were measured using a two-probe method on an electrical transport properties measurement system comprising a Keithley 2400 multiple-function source-meter. Mechanical property tests were carried out on an HS-3002C at a loading rate of 10% per minute. XRD data were collected with an X'Pert Pro (PANalytical) diffractometer using monochromatic Cu Kα1 radiation (λ = 1.5406 Å) at 40 kV. Confocal laser scanning microscopy observations were conducted on a Zeiss Lsm510 microscope, using a 488 nm laser to excite with a filtrate around 560 nm. XPS was carried out using a PHI 5000C ESCA system operated at 14.0 kV. Raman spectra were recorded on a Labram HRUV spectrometer operating at 632.8 nm.

Conflict of Interest: The authors declare no competing financial interest.

Acknowledgment. This work was funded by the National Natural Science Foundation of China (nos. 21325417 and 51173162) and State Key Laboratory for Modification of Chemical Fibers and Polymer Materials, Donghua University (no. LK1403).

Supporting Information Available: POM images of GO-MMT hybrids, SEM images of a surface section of a G-MMT fiber, and corresponding element mapping, cross-sections and fracture tips of G-MMT fibers under tension for typical mechanical measurements, mechanical properties and electrical conductivities of MMT-G fibers with different weight ratios, physical property changes of fibers during heating processing, SEM images showing the flexibility of the MMT-G (80/20) fibers, a full-view picture of the circuit constructed with an LED chip and MMT-G (10/90) fibers, and the recorded movies of combustion progress of the MMT-G film and neat graphene film. This material is available free of charge *via* the Internet at http://pubs.acs.org.

REFERENCES AND NOTES

1. Osada, M.; Sasaki, T. Two-Dimensional Dielectric Nanosheets: Novel Nanoelectronics from Nanocrystal Building Blocks. *Adv. Mater.* **2012**, *24*, 210–228.
2. Butler, S. Z.; Hollen, S. M.; Cao, L.; Cui, Y.; Gupta, J. A.; Gutiérrez, H. R.; Heinz, T. F.; Hong, S. S.; Huang, J.; Ismach, A. F.; *et al.* Progress, Challenges, and Opportunities in Two-Dimensional Materials beyond Graphene. *ACS Nano* **2013**, *7*, 2898–2926.
3. Koppens, F. H. L.; Mueller, T.; Avouris, P.; Ferrari, A. C.; Vitiello, M. S.; Polini, M. Photodetectors Based on Graphene, Other Two-Dimensional Materials and Hybrid Systems. *Nat. Nanotechnol.* **2014**, *9*, 780–793.
4. Xu, M.; Liang, T.; Shi, M.; Chen, H. Graphene-Like Two-Dimensional Materials. *Chem. Rev.* **2013**, *113*, 3766–3798.
5. Tang, Z.; Kotov, N. A.; Magonov, S.; Ozturk, B. Nanostructured Artificial Nacre. *Nat. Mater.* **2003**, *2*, 413–418.
6. Bonderer, L. J.; Studart, A. R.; Gauckler, L. J. Bioinspired Design and Assembly of Platelet Reinforced Polymer Films. *Science* **2008**, *319*, 1069–1073.
7. Coleman, J. N.; Lotya, M.; O'Neill, A.; Bergin, S. D.; King, P. J.; Khan, U.; Young, K.; Gaucher, A.; De, S.; Smith, R. J.; *et al.* Two-Dimensional Nanosheets Produced by Liquid Exfoliation of Layered Materials. *Science* **2011**, *331*, 568–571.
8. Yao, H.-B.; Tan, Z.-H.; Fang, H.-Y.; Yu, S.-H. Artificial Nacre-Like Bionanocomposite Films from the Self-Assembly of Chitosan–Montmorillonite Hybrid Building Blocks. *Angew. Chem., Int. Ed.* **2010**, *49*, 10127–10131.
9. Cote, L. J.; Kim, F.; Huang, J. Langmuir–Blodgett Assembly of Graphite Oxide Single Layers. *J. Am. Chem. Soc.* **2008**, *131*, 1043–1049.

10. Li, X.; Zhang, G.; Bai, X.; Sun, X.; Wang, X.; Wang, E.; Dai, H. Highly Conducting Graphene Sheets and Langmuir-Blodgett Films. *Nat. Nanotechnol.* **2008**, *3*, 538–542.
11. Wu, Z.-S.; Winter, A.; Chen, L.; Sun, Y.; Turchanin, A.; Feng, X.; Müllen, K. Three-Dimensional Nitrogen and Boron Co-doped Graphene for High-Performance All-Solid-State Supercapacitors. *Adv. Mater.* **2012**, *24*, 5130–5135.
12. Xu, Y.; Sheng, K.; Li, C.; Shi, G. Self-Assembled Graphene Hydrogel *via* a One-Step Hydrothermal Process. *ACS Nano* **2010**, *4*, 4324–4330.
13. Sun, H.; Xu, Z.; Gao, C. Multifunctional, Ultra-Flyweight, Synergistically Assembled Carbon Aerogels. *Adv. Mater.* **2013**, *25*, 2554–2560.
14. Vinod, S.; Tiwary, C. S.; Da Silva Autreto, P. A.; Taha-Tijerina, J.; Ozden, S.; Chipara, A. C.; Vajtai, R.; Galvao, D. S.; Narayanan, T. N.; Ajayan, P. M. Low-Density Three-Dimensional Foam Using Self-Reinforced Hybrid Two-Dimensional Atomic Layers. *Nat. Commun.* **2014**, *5*, 4541.
15. Liu, Z.; Li, Z.; Xu, Z.; Xia, Z.; Hu, X.; Kou, L.; Peng, L.; Wei, Y.; Gao, C. Wet-Spun Continuous Graphene Films. *Chem. Mater.* **2014**, *26*, 6786–6795.
16. Hu, X.; Xu, Z.; Liu, Z.; Gao, C. Liquid Crystal Self-Templating Approach to Ultrastrong and Tough Biomimic Composites. *Sci. Rep.* **2013**, *3*, 2374.
17. Xu, Z.; Gao, C. Graphene in Macroscopic Order: Liquid Crystals and Wet-Spun Fibers. *Acc. Chem. Res.* **2014**, *47*, 1267–1276.
18. Cheng, H.; Hu, C.; Zhao, Y.; Qu, L. Graphene Fiber: A New Material Platform for Unique Applications. *NPG Asia Mater.* **2014**, *6*, e113.
19. Xu, Z.; Gao, C. Graphene Chiral Liquid Crystals and Macroscopic Assembled Fibres. *Nat. Commun.* **2011**, *2*, 571.
20. Kou, L.; Huang, T.; Zheng, B.; Han, Y.; Zhao, X.; Gopalsamy, K.; Sun, H.; Gao, C. Coaxial Wet-Spun Yarn Supercapacitors for High-Energy Density and Safe Wearable Electronics. *Nat. Commun.* **2014**, *5*, 3754.
21. Xu, Z.; Sun, H.; Zhao, X.; Gao, C. Ultrastrong Fibers Assembled from Giant Graphene Oxide Sheets. *Adv. Mater.* **2013**, *25*, 188–193.
22. Weng, Z.; Xu, Z.; Gao, C. Highly Oxidized Graphene with Enhanced Fluorescence and Its Direct Fluorescence Visualization. *Sci. China Chem.* **2014**, *57*, 605–614.
23. Ferreira, A. U. C.; Poli, A. L.; Gessner, F.; Neumann, M. G.; Schmitt Cavalheiro, C. C. Interaction of Auramine O with Montmorillonite Clays. *J. Lumin.* **2013**, *136*, 63–67.
24. Ruzicka, B.; Zaccarelli, E. A Fresh Look at the Laponite Phase Diagram. *Soft Matter* **2011**, *7*, 1268–1286.
25. Tombácz, E.; Szekeres, M. Colloidal Behavior of Aqueous Montmorillonite Suspensions: The Specific Role of pH in the Presence of Indifferent Electrolytes. *Appl. Clay Sci.* **2004**, *27*, 75–94.
26. Pavlidou, S.; Papaspyrides, C. D. A Review on Polymer-Layered Silicate Nanocomposites. *Prog. Polym. Sci.* **2008**, *33*, 1119–1198.
27. Hedley, C. B.; Yuan, G.; Theng, B. K. G. Thermal Analysis of Montmorillonites Modified with Quaternary Phosphonium and Ammonium Surfactants. *Appl. Clay Sci.* **2007**, *35*, 180–188.
28. Rourke, J. P.; Pandey, P. A.; Moore, J. J.; Bates, M.; Kinloch, I. A.; Young, R. J.; Wilson, N. R. The Real Graphene Oxide Revealed: Stripping the Oxidative Debris from the Graphene-Like Sheets. *Angew. Chem., Int. Ed.* **2011**, *50*, 3173–3177.
29. Miaudet, P.; Badaire, S.; Maugey, M.; Derré, A.; Pichot, V.; Launois, P.; Poulin, P.; Zakri, C. Hot-Drawing of Single and Multiwall Carbon Nanotube Fibers for High Toughness and Alignment. *Nano Lett.* **2005**, *5*, 2212–2215.
30. Zhang, C.; Tjiu, W. W.; Fan, W.; Yang, Z.; Huang, S.; Liu, T. Aqueous Stabilization of Graphene Sheets Using Exfoliated Montmorillonite Nanoplatelets for Multifunctional Free-Standing Hybrid Films *via* Vacuum-Assisted Self-Assembly. *J. Mater. Chem.* **2011**, *21*, 18011–18017.
31. Losego, M. D.; Blitz, I. P.; Vaia, R. A.; Cahill, D. G.; Braun, P. V. Ultralow Thermal Conductivity in Organoclay Nanolaminates Synthesized *via* Simple Self-Assembly. *Nano Lett.* **2013**, *13*, 2215–2219.
32. Zhu, J.; Uhl, F. M.; Morgan, A. B.; Wilkie, C. A. Studies on the Mechanism by Which the Formation of Nanocomposites Enhances Thermal Stability. *Chem. Mater.* **2001**, *13*, 4649–4654.
33. Arora, A.; Choudhary, V.; Sharma, D. K. Effect of Clay Content and Clay/Surfactant on the Mechanical, Thermal and Barrier Properties of Polystyrene/Organoclay Nanocomposites. *J. Polym. Res.* **2011**, *18*, 843–857.
34. Liu, L.; Ryu, S.; Tomasik, M. R.; Stolyarova, E.; Jung, N.; Hybertsen, M. S.; Steigerwald, M. L.; Brus, L. E.; Flynn, G. W. Graphene Oxidation: Thickness-Dependent Etching and Strong Chemical Doping. *Nano Lett.* **2008**, *8*, 1965–1970.
35. Giannelis, E. P. Polymer Layered Silicate Nanocomposites. *Adv. Mater.* **1996**, *8*, 29–35.
36. LeBaron, P. C.; Wang, Z.; Pinnavaia, T. J. Polymer-Layered Silicate Nanocomposites: An Overview. *Appl. Clay Sci.* **1999**, *15*, 11–29.
37. Ray, S. S.; Yamada, K.; Okamoto, M.; Ogami, A.; Ueda, K. New Polylactide/Layered Silicate Nanocomposites. 3. High-Performance Biodegradable Materials. *Chem. Mater.* **2003**, *15*, 1456–1465.
38. Fredrickson, G. H.; Bicerano, J. Barrier Properties of Oriented Disk Composites. *J. Chem. Phys.* **1999**, *110*, 2181–2188.
39. Burnside, S. D.; Giannelis, E. P. Synthesis and Properties of New Poly(dimethylsiloxane) Nanocomposites. *Chem. Mater.* **1995**, *7*, 1597–1600.
40. Zeng, K.; Bai, Y. Improve the Gas Barrier Property of PET Film with Montmorillonite by *in Situ* Interlayer Polymerization. *Mater. Lett.* **2005**, *59*, 3348–3351.
41. Peng, L.; Xu, Z.; Liu, Z.; Wei, Y.; Sun, H.; Li, Z.; Zhao, X.; Gao, C. An Iron-Based Green Approach to 1-h Production of Single-Layer Graphene Oxide. *Nat. Commun.* **2015**, *6*, 5716.